Native mass spectrometry reveals binding interactions of SARS-CoV-2 PLpro with inhibitors and cellular targets

Virginia K. James[1], Rianna N. Godula[2], Jessica M. Perez[2], Josh T. Beckham,[3] Jamie P. Butalewicz[1], Sarah N. Sipe[1], Jon M. Huibregtse[2], Jennifer S. Brodbelt[1*]

[1]Department of Chemistry, The University of Texas at Austin, Austin, TX 78712
[2]Department of Molecular Biosciences, The University of Texas at Austin, Austin, TX 78712
[3]Freshman Research Initiative, The University of Texas at Austin, Austin, TX 78712

Abstract

Here we used native mass spectrometry (native MS) to probe a SARS-CoV protease, PLpro, which plays critical roles in coronavirus disease by affecting viral protein production and antagonizing host antiviral responses. Ultraviolet photodissociation (UVPD) and variable temperature electrospray ionization (vT ESI) were used to localize binding sites of PLpro inhibitors and revealed the stabilizing effects of inhibitors on protein tertiary structure. We compared PLpro from SARS-CoV-1 and SARS-CoV-2 in terms of inhibitor and ISG15 interactions to discern possible differences in protease function. A PLpro mutant lacking a single cysteine was used to localize inhibitor binding, and thermodynamic measurements revealed that inhibitor PR-619 stabilized the folded PLpro structure. These results will inform further development of PLpro as a therapeutic target against SARS-CoV-2 and other emerging coronaviruses.

Introduction:

As part of the non-structural protein 3 (nsp3) protein of SARS-CoV-2,[1] PLpro is required for generation of nsp1-4 by proteolytic cleavage of the orf1a polyprotein. [2] PLpro is an approximately 36 kDa domain within the much larger nsp3 protein.[3] In addition to generation of the nsp1-4 proteins, SARS-CoV-2 PLpro modulates host responses by antagonizing the function of ISG15, an interferon-induced ubiquitin-like protein. It does this by catalyzing the cleavage of the isopeptide bond that links the C-terminus of ISG15 to the ε-amino group of lysine side chains of host and viral proteins.[2] Consistent with this dual role of PLpro, the cleavage sites within the orf1a polyprotein bear striking amino acid similarity to the C-terminus of ISG15. Thus, therapeutic inhibition of PLpro would be expected to both disrupt viral protein production and restore the anti-viral activities of ISG15.[4]

Given its importance in disease progression, several avenues for PLpro inhibition have been explored. The active site of PLpro (defined in part by C111, H272, and D286 of the PLpro only domain) may be occupied by small molecules that inhibit protease activity, and several molecules such as GRL-0617[5] and its derivatives[6] have been shown to bind and inhibit PLpro, with x-ray crystal structures of the complexes available in some cases. Structures with other inhibitors, including rac5c and rac3k[7] and several nanomolar-affinity 2-phenylthiophenes compounds, have also been determined.[8] Crystal structures of PLpro•peptide inhibitor complexes have also been solved[9], as well as structures for PLpro bound to ISG15[2], ubiquitin[10] and dimeric ubiquitin.[10] Other methods such as nuclear magnetic resonance (NMR) have been used for validation of crystal structures[11] as well as to track PLpro inhibitors that disrupt the interaction between PLpro and ISG15.[5] Biological assays including *in vitro* inhibition experiments have shown successful inhibition of PLpro by many small molecule inhibitors such as 6-thioguanine,[12] PR-619[13] and many others.[14–20] IC_{50} measurements based on monitoring cleavage of the nsp domain site or a polyubiquitin protein in the absence and presence of inhibitors have been widely used to evaluate numerous inhibitors[19,21–24] and nanobodies.[25] As PLpro is a zinc binding protein, it may also be inhibited allosterically by ejection of zinc thus causing protein misfolding,[26] and a recent study found that several small molecule inhibitors can eject zinc from PLpro.[27]

Mass spectrometry (MS) has also emerged as a powerful tool for analysis of proteases such as PLpro, affording accurate masses of cleavage peptides and intact proteins. Liquid chromatography mass spectrometry analysis of tryptic digests of PLpro (i.e., bottom-up proteomics) has shown utility in assays for detecting SARS-CoV-2 via identification of peptides from the virus in complex matrices such as blood and urine,[28] and this method has also localized covalently bound inhibitors to PLpro.[27,29] Crosslinking mass

spectrometry revealed that interferon-induced ISG15 protein binds in a different region of PLpro compared to other ubiquitin and dimeric ubiquitin.[30] Analysis of intact, denatured PLpro (i.e. top-down proteomics) has been used to differentiate non-covalent and covalently bound inhibitors, especially when multiple inhibitors molecules are bound.[27] While these mass spectrometry techniques involving denatured proteins have been successful in characterizing covalently bound inhibitors, non-covalent interactions are not preserved under denaturing conditions and any information about protein tertiary structure is lost.

Native MS, which involves analyzing proteins in aqueous solutions of high ionic strength, is an attractive alternative as non-covalent interactions may be preserved as proteins are transported to the gas phase by electrospray ionization, allowing retention of protein conformations that resemble solution structures.[31–33] The scope of problems that native MS can solve has expanded with the emergence of other auxiliary methods, including collision induced unfolding (CIU) and collision cross section (CCS) measurements,[33,34] variable temperature electrospray ionization (vT-ESI),[35–37] and alternative MS/MS methods, such as ultraviolet photodissociation (UVPD).[38] vT-ESI allows determination of melting temperatures of proteins and protein complexes[36] and measurement of thermodynamic parameters associated with ligand binding.[37,39] UVPD has been used to localize inhibitor binding regions of proteins[40] and reveal unfolded/extended vs folded protein regions,[41] thus providing deeper insight into protein tertiary structure.

Native MS is well suited for examination of interactions between PLpro and inhibitors, particularly those that engage in non-covalent binding,[42] in addition to probing the interactions of PLpro and ISG15. Native MS has enabled the screening of many inhibitors to another SARS-CoV-2 protease, Mpro,[22,43–45] and to measure their effect on the thermodynamic parameters of Mpro.[39] Here we showcase the use of native MS to study interactions between PLpro, ISG15, and nsp domain cleavage sites and decipher the effects that small molecule inhibitors have on PLpro activity and tertiary structure stability.

Methods:

Materials

Equine heart myoglobin, bovine ubiquitin, acetonitrile, and ammonium acetate were purchased from Sigma-Aldrich (St. Louis, MO, USA). LC-MS grade water and methanol was purchased from Merck Millipore (Billerica, MA, USA). For experiments involving native-like charge states, proteins were diluted in a 100 mM ammonium acetate buffer to a final concentration of 10 µM and desalted with Micro Bio-

Spin™ P-6 Gel Columns (Bio-Rad Laboratories Inc., Hercules, CA). For experiments with denaturing conditions, proteins were diluted in a denaturing 1:1 water–methanol solution containing 0.1% formic acid to a final concentration of 10 µM without further purification. Small molecule inhibitors were purchased from Cayman Chemicals and used as received. MS1 spectra, structures and masses of the inhibitors are shown in **Figures S1-S2** and **Tables S1-S2,** and the MS/MS spectra of PR-619 are shown in **Figure S3**. For inhibitor binding experiments, 100 µM of inhibitor was added to 10 µM of PLpro in 100 mM ammonium acetate and incubated for 30 minutes at room temperature prior to ESI-MS analysis.

Protein expression and purification

All proteins were generated in house as previously described, with some modifications.[12] The PLpro domain (residues 1-315) was defined as residues 1283 to 1597 of the SARS-CoV-2 ORF1a polyprotein which is equivalent to residues 746 to 1060 of nsp3. The PLpro domain of SARS-CoV-1 (residues 1-315) was defined as residues 1541-1855 of that SARS-CoV-1 ORF1a polyprotein, which is equivalent to residues 723 to 1037 of Nsp3. All amino acid numbering that follows will be based on the isolated PLpro domains. SARs-CoV-2 PLpro WT and C111S mutant, PLpro from SARS-CoV-1, and Pro-ISG15-HA were purified as GST fusion proteins in BL21 *E. coli*. Overnight cultures were grown at 37 °C for all proteins. Cultures were diluted 1:20 and cultured with shaking for 2 hours at 37 °C. Expression of each protein was induced with 100 µM isopropyl β-D-1-thiogalactopyranoside (IPTG) overnight at 16 °C for all PLpro proteins and 3 hours at 30 °C for Pro-ISG15-HA. Cells were pelleted by centrifugation, resuspended in 10 mL PBS with 0.1% Triton X (Lysing Buffer), and sonicated for 1.5 minutes in 30 second intervals for lysing. Lysates were centrifuged at 10,000 x g for 10 minutes and supernatants were incubated with 100 µL of Glutathione Sepharose (GE Healthcare) and 1 mM phenylmethylsulfonyl (PMSF; Tocris) overnight with end-over-end rotation at 4 °C. Beads were washed three times with Lysis Buffer and three times subsequently with PC Buffer (50 mM Tris, 150 mM NaCl, 0.1% Triton X). Proteins were subjected to site-specific cleavage with PreScission Protease (GE Healthcare) to remove the GST tag. Beads were removed and the protein concentration in the supernatant was quantified by SDS-PAGE and Western blotting densitometry using a Licor Odyssey Imager. Protein sequences and monoisotopic masses are given in **Table S3**; note that all proteins retained a GPLGS leader sequence following protease cleavage. Masses of expected PLpro1, PLpro2 and PLpro2 C111S complexes are summarized in **Table S4**. Sequence alignment of PLpro1, PLpro2 and PLpro2 C111S is shown in **Figure S4**, and MS1 spectra of native and denatured PLpro are shown in **Figure S5**.

Instrumentation

Most experiments were performed on a Thermo Scientific™ Q Exactive™ HF-X quadrupole-Orbitrap mass spectrometer (Bremen, Germany) with Biopharma option, which was modified to perform ultraviolet photodissociation (UVPD) in the HCD cell by addition of a 500 Hz 193 nm Coherent® ExciStar excimer laser (Santa Cruz, CA) as previously described.[46,47] A variable temperature ESI source was interfaced with the mass spectrometer as previously described, allowing measurement of the impact of solution temperature on the charge state distributions of the proteins in the MS1 spectra.[37,41] Experiments involving some of the solutions containing protein complexes were performed on a prototype Q Exactive Plus Ultra High Mass Range (UHMR) Orbitrap mass spectrometer (Thermo Fisher Scientific, Bremen, Germany), which was optimized for the preservation of weak, non-covalent interactions. Ions were generated by nanoelectrospray ionization using Au/Pd-coated borosilicate emitters fabricated in-house and using a spray voltage of 0.8-1.2 kV. The C-trap gas pressure was set to 0.5 to 1.0, corresponding to a UHV gauge reading of around 1E-10 to 1.5E-10 mbar, respectively. Throughout the course of this study, some variations in charge state distributions of ions were observed for different solutions or when using the standard nanospray emitters versus the variable temperature source. Replicates of each category of experiment were collected on the same day to minimize these variations. For MS1 and MS2 experiments, 7,500 and 240,000 resolution settings were used, respectively.

Data Acquisition and Processing. Variable temperature ESI data was analyzed using a custom MATLAB R2020a script as previously described.[41] UVPD mass spectra were deconvoluted using Xtract in QualBrowser, and sequence coverage maps and fragment abundance plots were generated from the deconvoluted data using MS-TAFI.[48] A custom version of MS-TAFI was used to compare UVPD replicate data so that only fragment ions identified in at least two out of three replicates were retained and 10 ppm error tolerance was used. Crystal structures were visualized from previously published data (PBD numbers listed where applicable) using PyMol (PyMOL Molecular Graphics System, version 2.4 Schrödinger, LLC). CID_{50} values were determined by increasing the collisional activation voltage applied to disassemble a protein•inhibitor complex while monitoring the abundances of the apo protein and surviving protein•inhibitor complex. CID_{50} values were calculated in Origin(Pro), (2020b, OriginLab Corporation, Northampton, MA, USA.) using a Boltzmann sigmoidal function. LC-MS data was processed using Byonic.

Molecular docking: Predictions for the ability of PR-619 to covalently bind cysteines in PLpro were made with molecular docking software: GOLD (Genetic Optimization of Ligand Docking) from the Cambridge Crystallographic Data Centre CCDC, Cambridge, UK. The PDB: 7CJM crystal structure was analyzed through the Molprobity site (Duke University) to assess the quality of the crystallographic data and apply flips to

relevant Asn, Gln, and His residues. The PBD 7CJM structure has a Molprobity score of 1.69 representing high quality data. In preparation for the three separate docking runs (one of each of the cysteines of interest), the original, co-crystalized ligand in the structure was deleted. Chain A was used for docking and hydrogens were added to the protein structure in GOLD and the link atom for covalent docking was defined as the sulfur atom on the cysteine of interest (either C148, C260, or C270). For the PR-619 ligand, the structure was obtained from PubChem (CID: 2817763) as a .mol2 file and one of the cyano groups was removed and the exposed sulfur atom was defined as the linking atom of the ligand for the covalent interaction in GOLD. After docking, the top score from 10 genetic algorithm runs for each of the three runs was saved along with the binding poses for analysis.

Results and Discussion:

SARS-CoV-1 and SARS-CoV-2 PLpro display different affinities for cellular targets but not inhibitors

We used native MS to investigate the effects of inhibitors on PLpro and compare the outcomes for PLpro in SARS-CoV-1 (PLpro1) to SARS-CoV-2 (PLpro2). Under native MS conditions, all three variants of PLpro (PLpro1, PLpro2, and PLpro2 C111S) retained one zinc atom. PLpro1 has been shown to preferentially target ubiquitin chains, while PLpro2 targets the ubiquitin-like interferon-stimulated gene 15 protein (ISG15).[2] Both PLpro1 and PLpro2 bound monomeric ubiquitin with low affinity (**Figures S6-S7**). PLpro2 cleaved the ISG15 precursor (ProISG15) to generate the mature ISG15 carboxyl-terminus (**Figure S8**) and also bound ISG15 with high affinity (**Figure S7**); PLpro1 showed no binding to ISG15 (**Figure S6**). These results agree with prior reports that PLpro1 has lower affinity for ISG15 than does PLpro2[49] and that PLpro2 binds ISG15 with higher affinity than ubiquitin as ISG15 also interacts via a secondary site on PLpro2.[30] PLpro has 86% sequence conservation between SARS-CoV-1 and SARS-CoV-2 as shown in the sequence alignment in **Figure S4,** and while the catalytic site is conserved between the two viruses, differences emerge in the secondary binding site which accounts for the lower affinity of ISG15 for PLpro1.

The interaction of PLpro2 and ISG15 was localized by undertaking UVPD of the PLpro2●ISG15 complex, a method which has previously been show to map protein-ligand interactions based on variations in the abundances of fragment ions produced by apo versus holo proteins.[40] In essence, ligand binding results in formation of non-covalent interactions not present for the apo protein, typically leading to suppression of fragmentation of regions involved in the new interactions of the holo protein. Non-covalent interactions are preserved upon UVPD of the holo protein, preventing separation and release of

fragment ions even if individual backbone bonds are cleaved. UVPD of the PLpro2●ISG15 complex (14+) resulted in an array of PLpro2 sequence ions as well as ejection of ISG15 (**Figure S9a**). There is a broad decrease in abundances of sequence ions corresponding to backbone cleavages near the N- and C- termini of PLpro2 when comparing UVPD of PLpro2●ISG15 relative to apo PLpro2 (**Figure S9b-d**). As the active site residues reside near both the N (C111) and C termini (H272, D286), these results agree with the crystal structure of PLpro2●ISG15 (**Figure S9e**), in which ISG15 binds around the active site.

Although previous studies have extensively evaluated interactions of PLpro1 and PLpro2 with ubiquitin, ubiquitin-like proteins,[30,49] and various small molecule drug candidates,[5,17,21] few studies have compared binding of small molecules to both PLpro1 and PLpro2. We selected seven potential inhibitors and evaluated them for binding to PLpro2 (and single point mutant PLpro2 C111S, described later). Solutions containing PLpro2 and each of the small molecule ligands were screened by native MS, and four (SJB2-043, YM-155, K777, Jun9-72-2) exhibited low or no binding to PLpro2 (**Figure S10**) and were thus discarded from further analysis. Complexes between PLpro2 and three of the small molecules (PR-619, HY-17542, and GRL-0617) were detected as seen by mass shifts added to PLpro2 in the MS1 spectra (**Figure 1, S11**). These same small molecules also bound to PLpro1 (**Figure S12**) and PLpro2 C111S (**Figure S13**). Prior studies have reported no PLpro inhibition, lower IC_{50} values, and/or only partial inhibition for the low binding inhibitors (SJB2-043, YM-155, K777, Jun9-72-2) versus the high binding inhibitors (GRL-0617, HY-17542, PR-619) (**Tables S1-S2**).[5,13,21,50,51] The similarity in binding trends for PLpro1 and PLpro2 seems reasonable given that the catalytic triad (C111, H272 and D286) of the active site of PLpro is conserved between the two viruses, and these small molecules are not expected to bind other secondary sites on the protein.

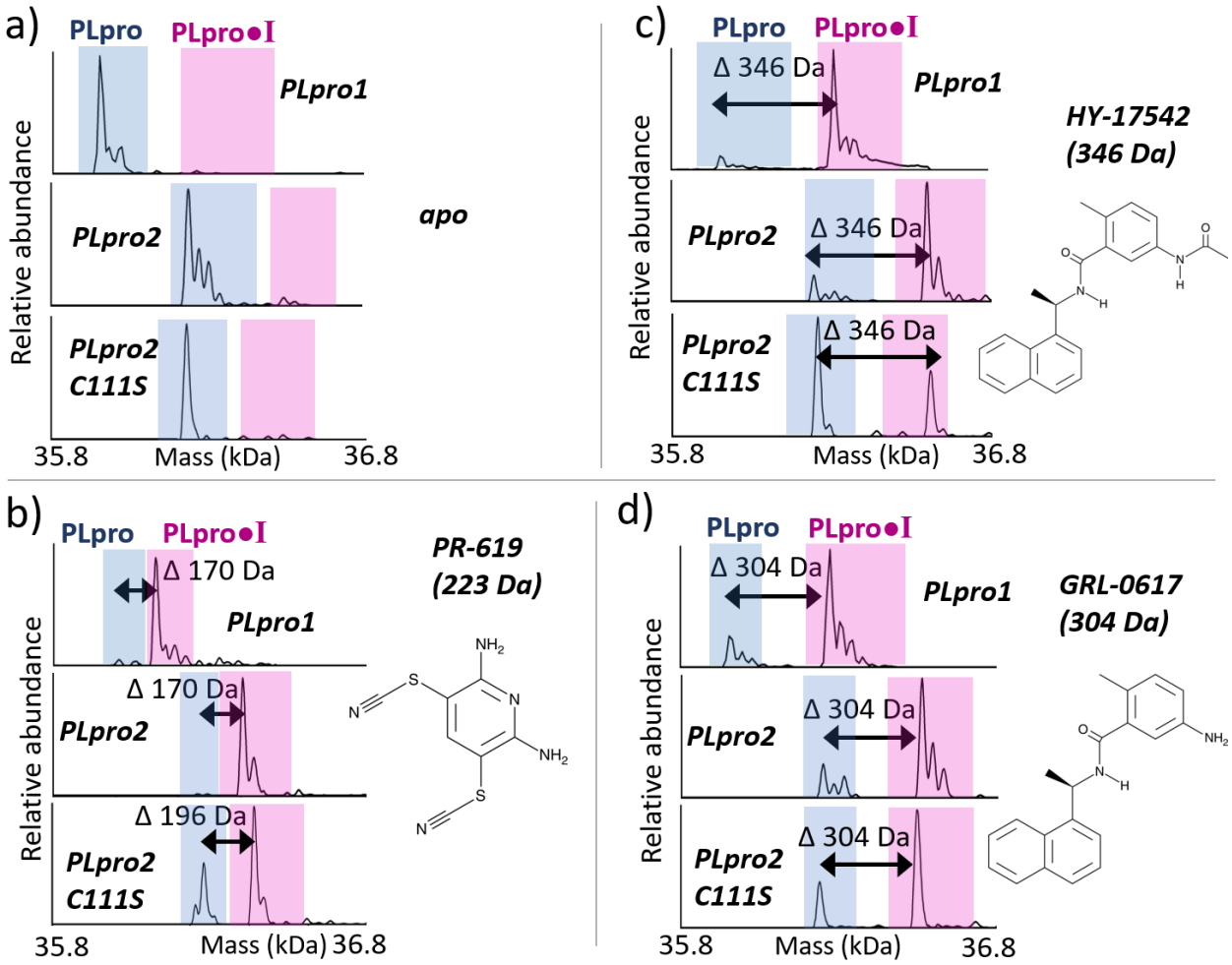

Figure 1. Deconvoluted mass spectra obtained for solutions containing 10 µM PLpro1, PLpro2, PLpro2 C111S (a) alone or with 100 µM inhibitor (I) including (b) PR-619, (c) HY-17542, or (d) GRL-0617 in 100 mM ammonium acetate. In parts a-d, PLpro1, PLpro2, and PLpro2 C111S are shown in the upper, middle, and lower panels, respectively. Non-deconvoluted MS1 spectra are shown in **Figures S11-13** for PLpro1, PLpro2, and PLpro2 C111S, respectively.

Inhibitor functional strength is commonly evaluated via IC_{50} values; however, we note a substantial degree of variability among IC_{50} values for PLpro inhibitors evaluated in different studies. For example, the reported IC_{50} values for PR-619 in inhibition of PLpro2 vary between 1.83 μM[13] to 6.1 μM,[21] thus highlighting the value of using a single type of assay for comparisons of PLpro inhibitors. Instead of measuring IC_{50} values, we measured CID_{50} values for each of the high binding inhibitors. CID_{50} values are derived from energy-variable collisional activation measurements; the CID_{50} value corresponds to the collision energy at which 50% of the PLpro•inhibitor complexes have dissociated, thus providing insight into the relative stabilities of the complexes in the gas phase.[52,53] Complexes containing GRL-0617 exhibited lower CID_{50} values than complexes containing HY-17542, suggesting that GRL-0617 is more weakly bound (**Figure 2**). The CID_{50} values for PLpro1•PR-619 and PLpro2•PR-619 were unmeasurable as PR-619 remained bound at all CID voltages, characteristic of a covalent binding mode. The CID_{50} values were similar for complexes containing PLpro1 or PLpro2, indicating no significant difference based on the sequences and structures adopted by these two PLpro proteins.

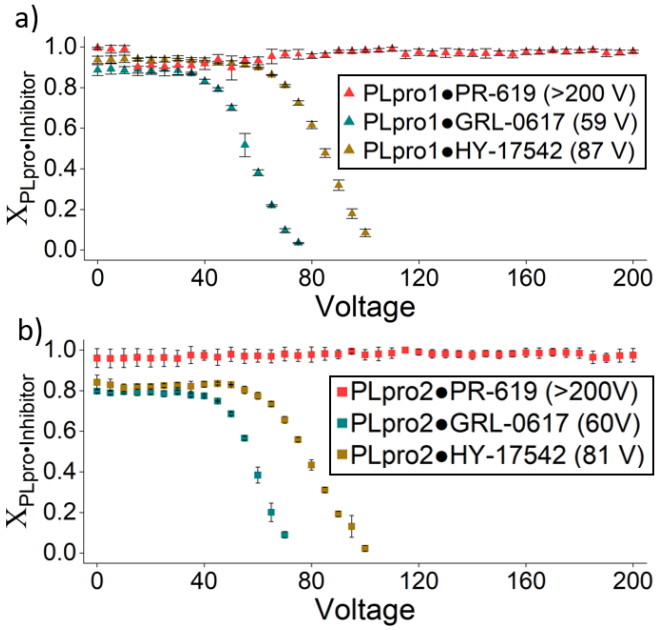

Figure 2. Energy-variable CID curves are shown for PLpro• inhibitor complexes containing GRL-0617, HY-17542 or PR-619 for (a) PLpro1 and (b) PLpro2. The derived CID_{50} values (±1 V) are summarized in the legend.

Next, we aimed to evaluate the inhibitor binding location and binding mode to PLpro2. The binding site of the most commonly studied inhibitor, GRL-0617, has been localized near the active site of PLpro2 based on several previously solved crystal structures,[5] and HY-17542 is expected to bind PLpro in a manner similar to GRL-0617 owing to their nearly identical structures (**Table S1**). Both GRL-0617 and HY-

17542 resulted in a mass shift equal to the mass of the ligand (**Figure 1c,d**) and bind with high affinity based on the prominence of the PLpro2•ligand complexes relative to apo PLpro2 in the MS1 spectra. For PR-619, PLpro2 (and PLpro1) displayed a mass shift of 170 Da (**Figure 1b**) rather than the mass of the intact ligand (223 Da). PR-619 has a unique structural motif containing two thiocyanate groups. Collisional induced dissociation of PR-619 yields fragment ions corresponding to the loss of one or two cyano groups from the thiocyanate motifs, resulting in product ions of *m/z* 196 and 170 (**Figure S3**). These results led us to postulate that PR-619 forms one or two disulfide bonds with one or two cysteine residues in PLpro2, in each case releasing one cyano group per new disulfide bond. Formation of two disulfide bonds with PLpro2 would correspond to a type of crosslinking.

While two previous studies evaluated interactions of PR-619 with PLpro2 and many others have used PR-619 for inhibition of related proteases, such as ubiquitin-specific proteases involved in cancer progression,[54,55] to our knowledge, no study has investigated the binding mechanism or location of PR-619 for deubiquitinating proteases. One important clue was obtained by examination of binding of PR-619 and the C111S mutant of PLpro2. This single point variant lacks the critical C111 in the active site triad, a site that is anticipated to be readily oxidized based on prior crystallographic evidence.[5] This C111S mutant alleviates the question of whether C111 is oxidized or reduced in PLpro2 and removes C111 as a binding site. PLpro2 C111S exhibits a mass shift equal to the mass of the inhibitor upon binding to HY-17542 and GRL-0617 (**Figure 1c,d, Figure S13**). The mass shift induced by PR-619 binding to PLpro2 C111S corresponds to 196 Da, not 170 Da as observed upon PR-619 binding to PLpro1 or PLpro2. The mass shift of 196 Da corresponds to the loss of a single cyano group from PR-619 (**Figure 1b, Figure S13d**). As PR-619 loses both cyano groups when binding to PLpro1 and PLpro2, we suspect that PR-619 forms disulfide bonds to two cysteine residues that are conserved between PLpro1 and PLpro2. There are eight conserved cysteine residues between PLpro1 and PLpro2 including C111 (confirmed as one of the PR-619 binding sites), C148, C189, C192, C224, C226, C260, and C270. Zinc remains bound to all complexes, suggesting that the four cysteines (C189, C192, C224, C226) that are known to bind zinc are not involved in binding to PR-619 and instead remain coordinated to zinc. Additionally, these four zinc-binding cysteines are spatially remote from the first confirmed binding site of PR-619 (C111), as far as 39-45 Å from C111 in the crystal structure of PLpro (PBD 7CJM, **Figure S14**). Crosslinking occurs when the two reactive residues in the protein crystal structure are within a reasonable tolerance (i.e., often 3-5 Å) of the distance spanned by crosslinking reagent itself.[56–59] The sulfur atoms of PR-619 are 9-10 Å apart. Three other conserved cysteine residues (C148, C260, and C270) are much closer to C111 with distances ranging from 11 Å (C148 and C270) to 16 Å (C260). Of these three cysteine residues, two (C148 and C260) are partially buried, thus

hindering ligand binding while C270 is more likely to bind to ligands as it is surface exposed (**Figure S14**). Therefore, C270 is the most likely second binding site of PR-619 as it is the closet solvent exposed cysteine residue similar to previous work that implicates C270 in the binding of other inhibitors.[60,61] This conclusion is further supported by molecular docking experiments, in which we performed docking of PR-619 with the loss of one cyano group to the PLpro2 C111S (PDB 7CJM). PR-619 binding to C148, C260, and C270 gave scores of -176.63, -80.34, and 50.09, respectively, where higher scores represent greater predicted ligand binding. The negative scores for the C148 and C260 suggest the inaccessibility of these residues as they are buried within the protein. These results suggest that C148 and C260 are not the second PR-619 binding site and agrees well with the assignment of C270 as the second PR-619 binding site.

To further investigate the inhibitor binding modes, the survival of the complexes was examined by denaturing the solutions containing PLpro2 after incubation with each inhibitor for 30 minutes and then examining the resulting mass spectra (**Figures S15** and **S16**). As expected, both GRL-0617 and HY-17542 are dislodged in the denaturing solutions (**Figure S15**), consistent with their non-covalent binding interactions. PR-619 remains largely bound to PLpro2 in the denaturing solution, indicating it is covalently bound (**Figure S16**). The overall abundance of PLpro2•PR-619 to apo PLpro2 in **Figure S16** suggests that ~40% of the protein is unbound after denaturation. As also seen in **Figure S16**, the ratio of PLpro2•PR-619 to apo PLpro2 decreases for the higher charge states for the denaturing solutions, indicating that strain from charge-induced protein elongation may further disrupt PR-619 binding despite the inhibitor being covalently bound.

The impact of the inhibitors on the interaction of PLpro2 and ISG15 was also evaluated. Incubation of PLpro2 with ISG15 results in abundant PLpro2●ISG15 complexes (**Figure 3, Figure S17**). All three inhibitors disrupt binding of ISG15 when added to the solutions containing PLpro2 and ISG15 (**Figure 3**). Prior in vitro results have reported inhibition of SARS-CoV-2 in the presence of three inhibitors including GRL-0617,[5,49] HY-17542,[20] and PR-619.[13,21] A previous NMR study also reported that GRL-0617 out-competed ISG15 to bind to PLpro2 when added to a solution containing PLpro2●ISG15.[5] Despite the differences in binding location and affinity, each inhibitor appears to disrupt binding of PLpro2 to ISG15.

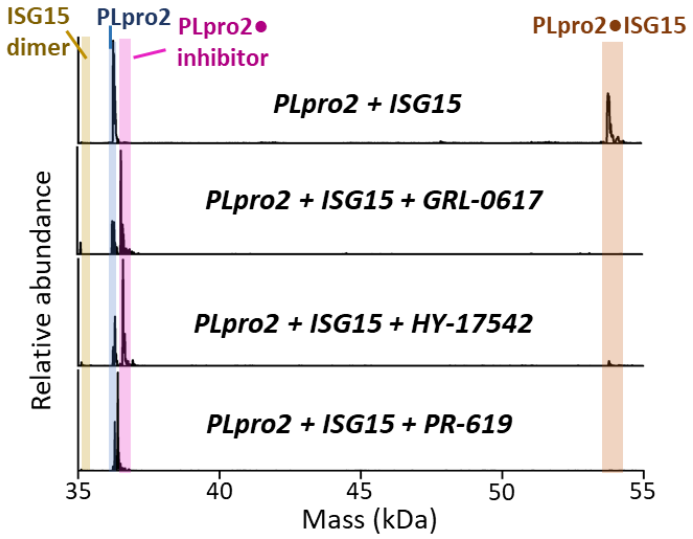

Figure 3. Deconvoluted mass spectra obtained for solutions containing both PLpro2 (10 µM) and ISG15 (10 µM) without or with three different inhibitors (100 µM) in 100 mM ammonium acetate. Non-deconvoluted spectra are shown in **Figure S17.**

Inhibitor PR-619 stabilizes PLpro tertiary structure.

To further probe the impact of inhibitor binding on PLpro2, UVPD was used to generate fragmentation patterns of apo PLpro2 and PLpro2• inhibitor complexes. UVPD has been used previously to reveal conformational variations in proteins, as fragmentation is generally enhanced in more flexible and less tightly organized regions. Ligand binding may also contribute to modulation of protein conformations because non-covalent interactions are re-organized during ligand binding. Networks of non-covalent interactions may suppress separation and release of fragment ions, an effect observed as a reduction in the abundances or number of fragment ions upon UVPD. The two non-covalent inhibitors, GRL-0617 and HY-17542, are released from PLpro2 during transfer to the collision cell, thus information about binding sites cannot be obtained by UVPD for complexes containing these weakly bound inhibitors. UVPD experiments were undertaken for PLpro bound to the covalent crosslinking inhibitor, PR-619, and the UVPD mass spectra and sequence maps of PLpro2 and PLpro2•PR-619 are shown in **Figures S18-19**. The number of fragment ions that originate from cleavages of different backbone positions for PLpro2 and PLpro2•PR-619 were counted and plotted as a function of backbone position in **Figure 4**. There was little variation in fragmentation observed upon UVPD of PLpro2 and PLpro2•PR-619 without any supplemental collisional activation (0 V), suggesting similar structures. In-source collisional activation may

be used prior to UVPD to induce protein unfolding,[62] and the resulting fragmentation patterns can be monitored to reveal regions of the protein that are disrupted.[41] While UVPD of PLpro2•PR-619 after no or low in-source collision activation resulted in insignificant differences in fragmentation compared to apo PLpro2, fragmentation increased for apo PLpro2 in the region spanning K105 to N144 after greater in-source collisional activation (200 V). This region of enhanced fragmentation of apo PLpro2 is demarcated on the sequence shown in **Figure 4b** and shaded on the crystal structure in **Figure 4c**. This region encompasses the suspected binding site of PLpro2•PR-619, suggesting that the suppression of UVPD fragmentation of PLpro2•PR-619 relative to apo PLpro2 indicates that PR-619 may stabilize the mid-section of PLpro. The loss of sequence coverage for PLpro2•PR-619 in the region between the C111 and the second suspected binding site (C270) further supports C270 as the second PR-619 binding site via a cross-linking mode that impedes fragmentation.

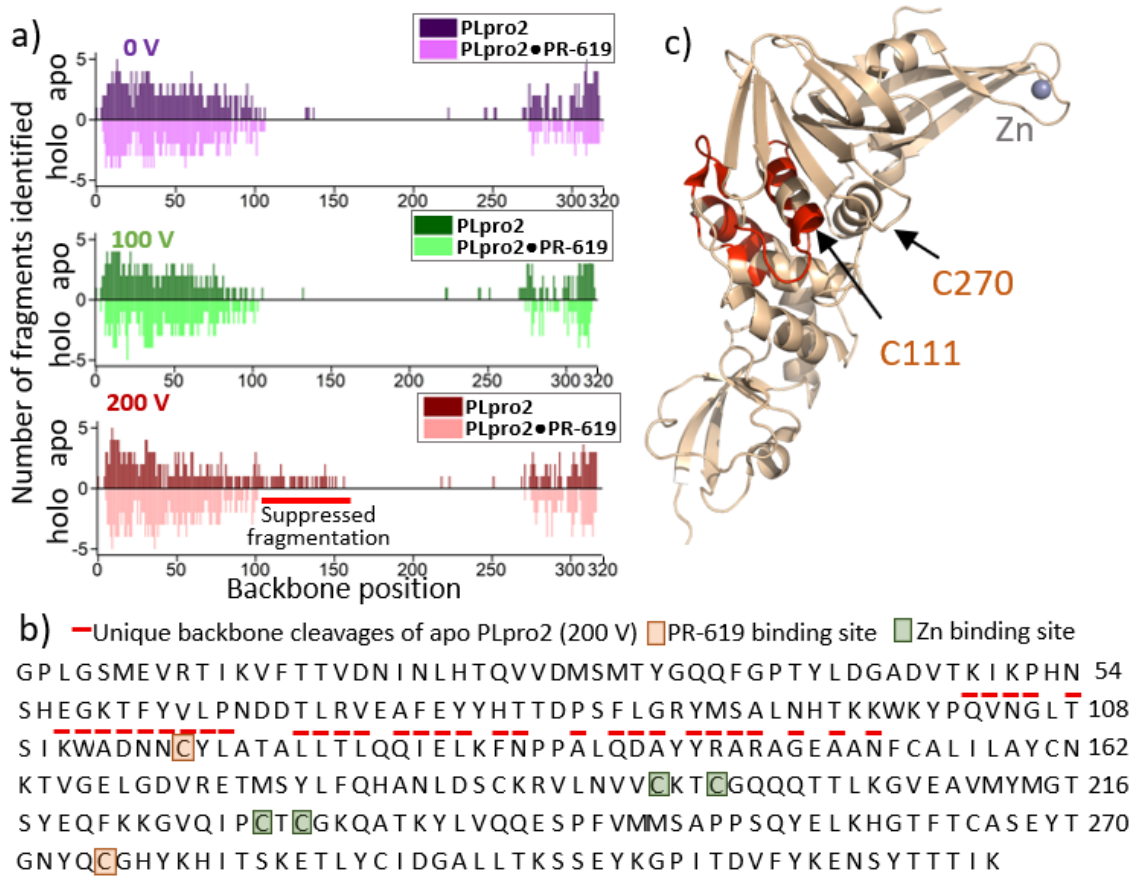

Figure 4. a) Mirror bar graphs showing the backbone cleavage sites that produce sequence ions apo PLpro2 (10+) and PLpro2●PR-619 (10+) upon UVPD (1 pulse, 2.5 mJ) when using 0, 100, or 200 V of in-source collisional activation. The dark bars representing fragmentation of apo PLpro2 are shown on the positive scale, and the light bars representing the fragmentation of PLpro2●PR-619 are shown on the negative scale. The heights of the bars represent the relative abundances of the fragment ions originating

from the backbone cleavage sites, allowing visualization of those regions for which fragmentation of PLpro2●PR-619 is suppressed relative to PLpro2. b) The backbone cleavage sites identified for apo PLpro2 that were not found for PLpro2●PR-619 are marked with red dashes above the residues on the sequence map of PLpro2, and c) shaded in red on the crystal structure (PDB 6XA9), indicating regions where fragmentation is suppressed in the PLpro2●PR-619 complex.

Variable temperature ESI (vT-ESI) analysis of apo PLpro2 and PLpro2•PR-619 was undertaken to evaluate variations in the thermodynamic stability of PLpro2 upon PR-619 binding and probe any structural stabilization imparted by inhibitor binding. For this method, the charge state distributions of the protein are monitored as a function of the temperature of the solution (**Figure 5** and **Figure S20**). vT-ESI of apo PLpro2 shows that the protein retains zinc even at high temperatures, suggesting that zinc is strongly bound. Zinc is only lost when the protein is sprayed from denaturing solutions (**Figure S15, 16**). The vT-ESI data shows that apo PLpro2 shifts to higher charge states as the temperature increases, consistent with protein elongation/unfolding which facilitates protonation of additional basic sites. In contrast, PLpro●PR-619 shows less variation in its charge state distribution as a function of solution temperature, indicative of greater stability of the folded PLpro2●PR-619 complex (**Figure 5**). These variable temperature ESI results affirm that the covalently bound PR-619 stabilizes the tertiary structure of PLpro2, which is congruent with a crosslinking binding mode.

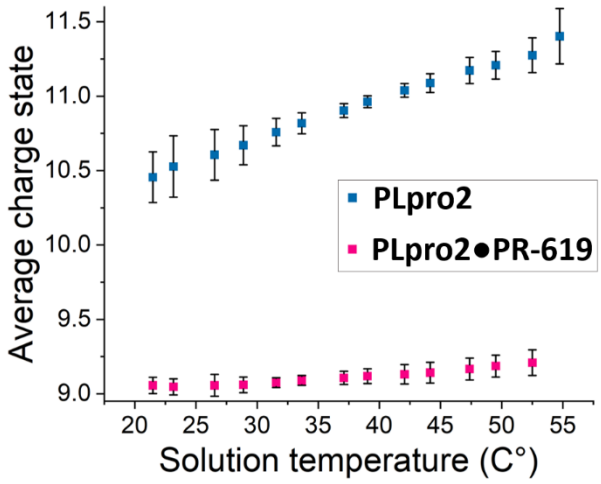

Figure 5. Impact of solution temperature on the average charge state of apo PLpro2 (10 µM in 100 mM ammonium acetate) and PLpro2●PR-619 (10 µm protein and 100 µm ligand in 100 mM ammonium acetate). MS1 spectra obtained at 20, 35, and 50 °C are shown in **Figure S20**.

Conclusions:

A comparison of PLpro from SARS-CoV-1 and SARS-CoV-2 was undertaken to evaluate the interaction of PLpro with inhibitors and ISG15. Using native MS, we confirmed that PLpro2 preferentially binds to ISG15 relative to PLpro1. At the same time, PLpro1 bound inhibitors designed for PLpro2. These results suggest that despite the differences in sequence conservation of PLpro between coronaviruses, the protease may still be a good therapeutic target for a broad range of coronaviruses.

We used ultraviolet photodissociation and a PLpro C111S mutant to localize the binding of PR-619, an inhibitor highlighted in several recent PLpro studies. We found that PR-619 acts as a covalent crosslinker, stabilizing the tertiary structure of PLpro as supported by vT-ESI-MS results. These results give insight into one of the binding mechanisms of PR-619, a widely used general inhibitor of deubiquitylating enzymes (DUBs).[55,63–67] Our findings are summarized in **Table 1**.

Table 1. Summary of interactions between PLpro proteins and inhibitors/cellular targets

	Ubiquitin	**ISG15**	**GRL-0617**	**HY-17542**	**PR-619[1]**
Binding mode:	Non-covalent	Non-covalent	Non-covalent	Non-covalent	Covalent binding to Cys
PLpro1	Minor	Minor	Prominent	Prominent	Crosslinking (C111 and C270)
PLpro2	Minor	Prominent	Prominent	Prominent	Crosslinking (C111 and C270)
PLpro2 C111S	N/A	N/A	Prominent	Prominent	Binding to C270

[1]Bond formation between PR-619 and cysteine displaces one cyano group of PR-619 per cysteine

Acknowledgments:

Funding from the National Institutes of Health (R35GM13965) and the Robert A. Welch Foundation (F-1155) to J.S.B. is gratefully acknowledged. This work was supported by a grant from the National Institutes for Allergy and Infectious Diseases (AI096090) to J.M.H.

References:

(1) Jahirul Islam, Md.; Nawal Islam, N.; Siddik Alom, Md.; Kabir, M.; Halim, M. A. A Review on Structural, Non-Structural, and Accessory Proteins of SARS-CoV-2: Highlighting Drug Target Sites. *Immunobiology* **2023**, *228* (1), 152302. https://doi.org/10.1016/j.imbio.2022.152302.

(2) Shin, D.; Mukherjee, R.; Grewe, D.; Bojkova, D.; Baek, K.; Bhattacharya, A.; Schulz, L.; Widera, M.; Mehdipour, A. R.; Tascher, G.; Geurink, P. P.; Wilhelm, A.; van der Heden van Noort, G. J.; Ovaa, H.; Müller, S.; Knobeloch, K.-P.; Rajalingam, K.; Schulman, B. A.; Cinatl, J.; Hummer, G.; Ciesek, S.; Dikic, I. Papain-like Protease Regulates SARS-CoV-2 Viral Spread and Innate Immunity. *Nature* **2020**, *587* (7835), 657–662. https://doi.org/10.1038/s41586-020-2601-5.

(3) Amin, Sk. A.; Banerjee, S.; Ghosh, K.; Gayen, S.; Jha, T. Protease Targeted COVID-19 Drug Discovery and Its Challenges: Insight into Viral Main Protease (Mpro) and Papain-like Protease (PLpro) Inhibitors. *Bioorganic & Medicinal Chemistry* **2021**, *29*, 115860. https://doi.org/10.1016/j.bmc.2020.115860.
(4) Liu, G.; Lee, J.-H.; Parker, Z. M.; Acharya, D.; Chiang, J. J.; van Gent, M.; Riedl, W.; Davis-Gardner, M. E.; Wies, E.; Chiang, C.; Gack, M. U. ISG15-Dependent Activation of the Sensor MDA5 Is Antagonized by the SARS-CoV-2 Papain-like Protease to Evade Host Innate Immunity. *Nat Microbiol* **2021**, *6* (4), 467–478. https://doi.org/10.1038/s41564-021-00884-1.
(5) Fu, Z.; Huang, B.; Tang, J.; Liu, S.; Liu, M.; Ye, Y.; Liu, Z.; Xiong, Y.; Zhu, W.; Cao, D.; Li, J.; Niu, X.; Zhou, H.; Zhao, Y. J.; Zhang, G.; Huang, H. The Complex Structure of GRL0617 and SARS-CoV-2 PLpro Reveals a Hot Spot for Antiviral Drug Discovery. *Nat Commun* **2021**, *12* (1), 488. https://doi.org/10.1038/s41467-020-20718-8.
(6) Sanders, B. C.; Pokhrel, S.; Labbe, A. D.; Mathews, I. I.; Cooper, C. J.; Davidson, R. B.; Phillips, G.; Weiss, K. L.; Zhang, Q.; O'Neill, H.; Kaur, M.; Schmidt, J. G.; Reichard, W.; Surendranathan, S.; Parvathareddy, J.; Phillips, L.; Rainville, C.; Sterner, D. E.; Kumaran, D.; Andi, B.; Babnigg, G.; Moriarty, N. W.; Adams, P. D.; Joachimiak, A.; Hurst, B. L.; Kumar, S.; Butt, T. R.; Jonsson, C. B.; Ferrins, L.; Wakatsuki, S.; Galanie, S.; Head, M. S.; Parks, J. M. Potent and Selective Covalent Inhibition of the Papain-like Protease from SARS-CoV-2. *Nat Commun* **2023**, *14* (1), 1733. https://doi.org/10.1038/s41467-023-37254-w.
(7) Calleja, D. J.; Kuchel, N.; Lu, B. G. C.; Birkinshaw, R. W.; Klemm, T.; Doerflinger, M.; Cooney, J. P.; Mackiewicz, L.; Au, A. E.; Yap, Y. Q.; Blackmore, T. R.; Katneni, K.; Crighton, E.; Newman, J.; Jarman, K. E.; Call, M. J.; Lechtenberg, B. C.; Czabotar, P. E.; Pellegrini, M.; Charman, S. A.; Lowes, K. N.; Mitchell, J. P.; Nachbur, U.; Lessene, G.; Komander, D. Insights Into Drug Repurposing, as Well as Specificity and Compound Properties of Piperidine-Based SARS-CoV-2 PLpro Inhibitors. *Frontiers in Chemistry* **2022**, *10*.
(8) Shen, Z.; Ratia, K.; Cooper, L.; Kong, D.; Lee, H.; Kwon, Y.; Li, Y.; Alqarni, S.; Huang, F.; Dubrovskyi, O.; Rong, L.; Thatcher, G. R. J.; Xiong, R. Design of SARS-CoV-2 PLpro Inhibitors for COVID-19 Antiviral Therapy Leveraging Binding Cooperativity. *J. Med. Chem.* **2022**, *65* (4), 2940–2955. https://doi.org/10.1021/acs.jmedchem.1c01307.
(9) Rut, W.; Lv, Z.; Zmudzinski, M.; Patchett, S.; Nayak, D.; Snipas, S. J.; El Oualid, F.; Huang, T. T.; Bekes, M.; Drag, M.; Olsen, S. K. Activity Profiling and Crystal Structures of Inhibitor-Bound SARS-CoV-2 Papain-like Protease: A Framework for Anti–COVID-19 Drug Design. *Science Advances* **2020**, *6* (42), eabd4596. https://doi.org/10.1126/sciadv.abd4596.
(10) Vliet, V. J. E. van; Huynh, N.; Palà, J.; Patel, A.; Singer, A.; Slater, C.; Chung, J.; Huizen, M. van; Teyra, J.; Miersch, S.; Luu, G.-K.; Ye, W.; Sharma, N.; Ganaie, S. S.; Russell, R.; Chen, C.; Maynard, M.; Amarasinghe, G. K.; Mark, B. L.; Kikkert, M.; Sidhu, S. S. Ubiquitin Variants Potently Inhibit SARS-CoV-2 PLpro and Viral Replication via a Novel Site Distal to the Protease Active Site. *PLOS Pathogens* **2022**, *18* (12), e1011065. https://doi.org/10.1371/journal.ppat.1011065.
(11) Napolitano, V.; Dabrowska, A.; Schorpp, K.; Mourão, A.; Barreto-Duran, E.; Benedyk, M.; Botwina, P.; Brandner, S.; Bostock, M.; Chykunova, Y.; Czarna, A.; Dubin, G.; Fröhlich, T.; Hölscher, M.; Jedrysik, M.; Matsuda, A.; Owczarek, K.; Pachota, M.; Plettenburg, O.; Potempa, J.; Rothenaigner, I.; Schlauderer, F.; Slysz, K.; Szczepanski, A.; Greve-Isdahl Mohn, K.; Blomberg, B.; Sattler, M.; Hadian, K.; Popowicz, G. M.; Pyrc, K. Acriflavine, a Clinically Approved Drug, Inhibits SARS-CoV-2 and Other Betacoronaviruses. *Cell Chemical Biology* **2022**, *29* (5), 774-784.e8. https://doi.org/10.1016/j.chembiol.2021.11.006.
(12) Swaim, C. D.; Dwivedi, V.; Perng, Y.-C.; Zhao, X.; Canadeo, L. A.; Harastani, H. H.; Darling, T. L.; Boon, A. C. M.; Lenschow, D. J.; Kulkarni, V.; Huibregtse, J. M. 6-Thioguanine Blocks SARS-CoV-2

Replication by Inhibition of PLpro. *iScience* **2021**, *24* (10), 103213. https://doi.org/10.1016/j.isci.2021.103213.
(13) Große, M.; Setz, C.; Rauch, P.; Auth, J.; Morokutti-Kurz, M.; Temchura, V.; Schubert, U. Inhibitors of Deubiquitinating Enzymes Interfere with the SARS-CoV-2 Papain-like Protease and Block Virus Replication In Vitro. *Viruses* **2022**, *14* (7), 1404. https://doi.org/10.3390/v14071404.
(14) Narayanan, A.; Narwal, M.; Majowicz, S. A.; Varricchio, C.; Toner, S. A.; Ballatore, C.; Brancale, A.; Murakami, K. S.; Jose, J. Identification of SARS-CoV-2 Inhibitors Targeting Mpro and PLpro Using in-Cell-Protease Assay. *Commun Biol* **2022**, *5* (1), 1–17. https://doi.org/10.1038/s42003-022-03090-9.
(15) Protić, S.; Kaličanin, N.; Sencanski, M.; Prodanović, O.; Milicevic, J.; Perovic, V.; Paessler, S.; Prodanović, R.; Glisic, S. In Silico and In Vitro Inhibition of SARS-CoV-2 PLpro with Gramicidin D. *International Journal of Molecular Sciences* **2023**, *24* (3), 1955. https://doi.org/10.3390/ijms24031955.
(16) Lewis, D. S. M.; Ho, J.; Wills, S.; Kawall, A.; Sharma, A.; Chavada, K.; Ebert, M. C. C. J. C.; Evoli, S.; Singh, A.; Rayalam, S.; Mody, V.; Taval, S. Aloin Isoforms (A and B) Selectively Inhibits Proteolytic and Deubiquitinating Activity of Papain like Protease (PLpro) of SARS-CoV-2 in Vitro. *Sci Rep* **2022**, *12* (1), 2145. https://doi.org/10.1038/s41598-022-06104-y.
(17) Kulandaisamy, R.; Kushwaha, T.; Dalal, A.; Kumar, V.; Singh, D.; Baswal, K.; Sharma, P.; Praneeth, K.; Jorwal, P.; Kayampeta, S. R.; Sharma, T.; Maddur, S.; Kumar, M.; Kumar, S.; Polamarasetty, A.; Singh, A.; Sehgal, D.; Gholap, S. L.; Appaiahgari, M. B.; Katika, M. R.; Inampudi, K. K. Repurposing of FDA Approved Drugs Against SARS-CoV-2 Papain-Like Protease: Computational, Biochemical, and in Vitro Studies. *Front Microbiol* **2022**, *13*, 877813. https://doi.org/10.3389/fmicb.2022.877813.
(18) Loffredo, M.; Lucero, H.; Chen, D.-Y.; O'Connell, A.; Bergqvist, S.; Munawar, A.; Bandara, A.; De Graef, S.; Weeks, S. D.; Douam, F.; Saeed, M.; Munawar, A. H. The In-Vitro Effect of Famotidine on SARS-CoV-2 Proteases and Virus Replication. *Sci Rep* **2021**, *11* (1), 5433. https://doi.org/10.1038/s41598-021-84782-w.
(19) Klemm, T.; Ebert, G.; Calleja, D. J.; Allison, C. C.; Richardson, L. W.; Bernardini, J. P.; Lu, B. G.; Kuchel, N. W.; Grohmann, C.; Shibata, Y.; Gan, Z. Y.; Cooney, J. P.; Doerflinger, M.; Au, A. E.; Blackmore, T. R.; van der Heden van Noort, G. J.; Geurink, P. P.; Ovaa, H.; Newman, J.; Riboldi-Tunnicliffe, A.; Czabotar, P. E.; Mitchell, J. P.; Feltham, R.; Lechtenberg, B. C.; Lowes, K. N.; Dewson, G.; Pellegrini, M.; Lessene, G.; Komander, D. Mechanism and Inhibition of the Papain-like Protease, PLpro, of SARS-CoV-2. *The EMBO Journal* **2020**, *39* (18), e106275. https://doi.org/10.15252/embj.2020106275.
(20) Cho, H.; Kim, Y. J.; Chae, J.-W.; Meyer, M. R.; Kim, S. K.; Ryu, C. S. In Vitro Metabolic Characterization of the SARS-CoV-2 Papain-like Protease Inhibitors GRL0617 and HY-17542. *Frontiers in Pharmacology* **2023**, *14*.
(21) Cho, C.-C.; Li, S. G.; Lalonde, T. J.; Yang, K. S.; Yu, G.; Qiao, Y.; Xu, S.; Ray Liu, W. Drug Repurposing for the SARS-CoV-2 Papain-Like Protease. *ChemMedChem* **2022**, *17* (1), e202100455. https://doi.org/10.1002/cmdc.202100455.
(22) Ma, C.; Hu, Y.; Townsend, J. A.; Lagarias, P. I.; Marty, M. T.; Kolocouris, A.; Wang, J. Ebselen, Disulfiram, Carmofur, PX-12, Tideglusib, and Shikonin Are Nonspecific Promiscuous SARS-CoV-2 Main Protease Inhibitors. *ACS Pharmacol. Transl. Sci.* **2020**, *3* (6), 1265–1277. https://doi.org/10.1021/acsptsci.0c00130.
(23) Freitas, B. T.; Durie, I. A.; Murray, J.; Longo, J. E.; Miller, H. C.; Crich, D.; Hogan, R. J.; Tripp, R. A.; Pegan, S. D. Characterization and Noncovalent Inhibition of the Deubiquitinase and deISGylase Activity of SARS-CoV-2 Papain-Like Protease. *ACS Infect. Dis.* **2020**, *6* (8), 2099–2109. https://doi.org/10.1021/acsinfecdis.0c00168.
(24) Zhao, Y.; Du, X.; Duan, Y.; Pan, X.; Sun, Y.; You, T.; Han, L.; Jin, Z.; Shang, W.; Yu, J.; Guo, H.; Liu, Q.; Wu, Y.; Peng, C.; Wang, J.; Zhu, C.; Yang, X.; Yang, K.; Lei, Y.; Guddat, L. W.; Xu, W.; Xiao, G.; Sun, L.;

Zhang, L.; Rao, Z.; Yang, H. High-Throughput Screening Identifies Established Drugs as SARS-CoV-2 PLpro Inhibitors. *Protein Cell* **2021**, *12* (11), 877–888. https://doi.org/10.1007/s13238-021-00836-9.

(25) Armstrong, L. A.; Lange, S. M.; Cesare, V. D.; Matthews, S. P.; Nirujogi, R. S.; Cole, I.; Hope, A.; Cunningham, F.; Toth, R.; Mukherjee, R.; Bojkova, D.; Gruber, F.; Gray, D.; Wyatt, P. G.; Cinatl, J.; Dikic, I.; Davies, P.; Kulathu, Y. Biochemical Characterization of Protease Activity of Nsp3 from SARS-CoV-2 and Its Inhibition by Nanobodies. *PLOS ONE* **2021**, *16* (7), e0253364. https://doi.org/10.1371/journal.pone.0253364.

(26) Maiti, B. K. Can Papain-like Protease Inhibitors Halt SARS-CoV-2 Replication? *ACS Pharmacol. Transl. Sci.* **2020**, *3* (5), 1017–1019. https://doi.org/10.1021/acsptsci.0c00093.

(27) Sargsyan, K.; Lin, C.-C.; Chen, T.; Grauffel, C.; Chen, Y.-P.; Yang, W.-Z.; S. Yuan, H.; Lim, C. Multi-Targeting of Functional Cysteines in Multiple Conserved SARS-CoV-2 Domains by Clinically Safe Zn-Ejectors. *Chemical Science* **2020**, *11* (36), 9904–9909. https://doi.org/10.1039/D0SC02646H.

(28) Lima, N. M.; Fernandes, B. L. M.; Alves, G. F.; de Souza, J. C. Q.; Siqueira, M. M.; Patrícia do Nascimento, M.; Moreira, O. B. O.; Sussulini, A.; de Oliveira, M. A. L. Mass Spectrometry Applied to Diagnosis, Prognosis, and Therapeutic Targets Identification for the Novel Coronavirus SARS-CoV-2: A Review. *Analytica Chimica Acta* **2022**, *1195*, 339385. https://doi.org/10.1016/j.aca.2021.339385.

(29) Yu, W.; Zhao, Y.; Ye, H.; Wu, N.; Liao, Y.; Chen, N.; Li, Z.; Wan, N.; Hao, H.; Yan, H.; Xiao, Y.; Lai, M. Structure-Based Design of a Dual-Targeted Covalent Inhibitor Against Papain-like and Main Proteases of SARS-CoV-2. *J. Med. Chem.* **2022**, *65* (24), 16252–16267. https://doi.org/10.1021/acs.jmedchem.2c00954.

(30) Wydorski, P. M.; Osipiuk, J.; Lanham, B. T.; Tesar, C.; Endres, M.; Engle, E.; Jedrzejczak, R.; Mullapudi, V.; Michalska, K.; Fidelis, K.; Fushman, D.; Joachimiak, A.; Joachimiak, L. A. Dual Domain Recognition Determines SARS-CoV-2 PLpro Selectivity for Human ISG15 and K48-Linked Di-Ubiquitin. *Nat Commun* **2023**, *14* (1), 2366. https://doi.org/10.1038/s41467-023-38031-5.

(31) Wu, D.; Robinson, C. V. Native Top-Down Mass Spectrometry Reveals a Role for Interfacial Glycans on Therapeutic Cytokine and Hormone Assemblies. *Angewandte Chemie International Edition n/a* (n/a). https://doi.org/10.1002/anie.202213170.

(32) Wang, H.; Eschweiler, J.; Cui, W.; Zhang, H.; Frieden, C.; Ruotolo, B. T.; Gross, M. L. Native Mass Spectrometry, Ion Mobility, Electron-Capture Dissociation, and Modeling Provide Structural Information for Gas-Phase Apolipoprotein E Oligomers. *J. Am. Soc. Mass Spectrom.* **2019**, *30* (5), 876–885. https://doi.org/10.1007/s13361-019-02148-z.

(33) Gadkari, V. V.; Ramírez, C. R.; Vallejo, D. D.; Kurulugama, R. T.; Fjeldsted, J. C.; Ruotolo, B. T. Enhanced Collision Induced Unfolding and Electron Capture Dissociation of Native-like Protein Ions. *Anal. Chem.* **2020**, *92* (23), 15489–15496. https://doi.org/10.1021/acs.analchem.0c03372.

(34) Lantz, C.; Lopez, J.; Goring, A. K.; Zenaidee, M. A.; Biggs, K.; Whitelegge, J. P.; Ogorzalek Loo, R. R.; Klärner, F.-G.; Schrader, T.; Bitan, G.; Loo, J. A. Characterization of Molecular Tweezer Binding on α-Synuclein with Native Top-Down Mass Spectrometry and Ion Mobility-Mass Spectrometry Reveals a Mechanism for Aggregation Inhibition. *J. Am. Soc. Mass Spectrom.* **2023**, *34* (12), 2739–2747. https://doi.org/10.1021/jasms.3c00281.

(35) Cong, X.; Liu, Y.; Liu, W.; Liang, X.; Russell, D. H.; Laganowsky, A. Determining Membrane Protein–Lipid Binding Thermodynamics Using Native Mass Spectrometry. *J. Am. Chem. Soc.* **2016**, *138* (13), 4346–4349. https://doi.org/10.1021/jacs.6b01771.

(36) Walker, T. E.; Shirzadeh, M.; Sun, H. M.; McCabe, J. W.; Roth, A.; Moghadamchargari, Z.; Clemmer, D. E.; Laganowsky, A.; Rye, H.; Russell, D. H. Temperature Regulates Stability, Ligand Binding (Mg2+ and ATP), and Stoichiometry of GroEL–GroES Complexes. *J. Am. Chem. Soc.* **2022**, *144* (6), 2667–2678. https://doi.org/10.1021/jacs.1c11341.

(37) McCabe, J. W.; Shirzadeh, M.; Walker, T. E.; Lin, C.-W.; Jones, B. J.; Wysocki, V. H.; Barondeau, D. P.; Clemmer, D. E.; Laganowsky, A.; Russell, D. H. Variable-Temperature Electrospray Ionization for Temperature-Dependent Folding/Refolding Reactions of Proteins and Ligand Binding. *Anal. Chem.* **2021**, *93* (18), 6924–6931. https://doi.org/10.1021/acs.analchem.1c00870.

(38) Rachel Mehaffey, M.; Ahn, Y.-C.; D. Rivera, D.; W. Thomas, P.; Cheng, Z.; W. Crowder, M.; F. Pratt, R.; Fast, W.; S. Brodbelt, J. Elusive Structural Changes of New Delhi Metallo-β-Lactamase Revealed by Ultraviolet Photodissociation Mass Spectrometry. *Chemical Science* **2020**, *11* (33), 8999–9010. https://doi.org/10.1039/D0SC02503H.

(39) Butalewicz, J.; Sipe, S.; Juetten, K.; James, V.; Meek, T.; Brodbelt, J. Insights into the Main Protease of SARS-CoV-2: Thermodynamic Analysis, Structural Characterization, and the Impact of Inhibitors. ChemRxiv November 6, 2023. https://doi.org/10.26434/chemrxiv-2023-lgv9f.

(40) O'Brien, J. P.; Li, W.; Zhang, Y.; Brodbelt, J. S. Characterization of Native Protein Complexes Using Ultraviolet Photodissociation Mass Spectrometry. *J. Am. Chem. Soc.* **2014**, *136* (37), 12920–12928. https://doi.org/10.1021/ja505217w.

(41) Sipe, S. N.; Lancaster, E. B.; Butalewicz, J. P.; Whitman, C. P.; Brodbelt, J. S. Symmetry of 4-Oxalocrotonate Tautomerase Trimers Influences Unfolding and Fragmentation in the Gas Phase. *J. Am. Chem. Soc.* **2022**, *144* (27), 12299–12309. https://doi.org/10.1021/jacs.2c03564.

(42) Osipiuk, J.; Azizi, S.-A.; Dvorkin, S.; Endres, M.; Jedrzejczak, R.; Jones, K. A.; Kang, S.; Kathayat, R. S.; Kim, Y.; Lisnyak, V. G.; Maki, S. L.; Nicolaescu, V.; Taylor, C. A.; Tesar, C.; Zhang, Y.-A.; Zhou, Z.; Randall, G.; Michalska, K.; Snyder, S. A.; Dickinson, B. C.; Joachimiak, A. Structure of Papain-like Protease from SARS-CoV-2 and Its Complexes with Non-Covalent Inhibitors. *Nat Commun* **2021**, *12* (1), 743. https://doi.org/10.1038/s41467-021-21060-3.

(43) Sacco, M. D.; Ma, C.; Lagarias, P.; Gao, A.; Townsend, J. A.; Meng, X.; Dube, P.; Zhang, X.; Hu, Y.; Kitamura, N.; Hurst, B.; Tarbet, B.; Marty, M. T.; Kolocouris, A.; Xiang, Y.; Chen, Y.; Wang, J. Structure and Inhibition of the SARS-CoV-2 Main Protease Reveal Strategy for Developing Dual Inhibitors against Mpro and Cathepsin L. *Science Advances* **2020**, *6* (50), eabe0751. https://doi.org/10.1126/sciadv.abe0751.

(44) Ma, C.; Sacco, M. D.; Hurst, B.; Townsend, J. A.; Hu, Y.; Szeto, T.; Zhang, X.; Tarbet, B.; Marty, M. T.; Chen, Y.; Wang, J. Boceprevir, GC-376, and Calpain Inhibitors II, XII Inhibit SARS-CoV-2 Viral Replication by Targeting the Viral Main Protease. *Cell Res* **2020**, *30* (8), 678–692. https://doi.org/10.1038/s41422-020-0356-z.

(45) El-Baba, T. J.; Lutomski, C. A.; Kantsadi, A. L.; Malla, T. R.; John, T.; Mikhailov, V.; Bolla, J. R.; Schofield, C. J.; Zitzmann, N.; Vakonakis, I.; Robinson, C. V. Allosteric Inhibition of the SARS-CoV-2 Main Protease: Insights from Mass Spectrometry Based Assays**. *Angewandte Chemie International Edition* **2020**, *59* (52), 23544–23548. https://doi.org/10.1002/anie.202010316.

(46) Sanders, J. D.; Shields, S. W.; Escobar, E. E.; Lanzillotti, M. B.; Butalewicz, J. P.; James, V. K.; Blevins, M. S.; Sipe, S. N.; Brodbelt, J. S. Enhanced Ion Mobility Separation and Characterization of Isomeric Phosphatidylcholines Using Absorption Mode Fourier Transform Multiplexing and Ultraviolet Photodissociation Mass Spectrometry. *Anal. Chem.* **2022**, *94* (10), 4252–4259. https://doi.org/10.1021/acs.analchem.1c04711.

(47) Blevins, M. S.; Juetten, K. J.; James, V. K.; Butalewicz, J. P.; Escobar, E. E.; Lanzillotti, M. B.; Sanders, J. D.; Fort, K. L.; Brodbelt, J. S. Nanohydrophobic Interaction Chromatography Coupled to Ultraviolet Photodissociation Mass Spectrometry for the Analysis of Intact Proteins in Low Charge States. *J. Proteome Res.* **2022**, *21* (10), 2493–2503. https://doi.org/10.1021/acs.jproteome.2c00450.

(48) Juetten, K. J.; Brodbelt, J. S. MS-TAFI: A Tool for the Analysis of Fragment Ions Generated from Intact Proteins. *J. Proteome Res.* **2023**, *22* (2), 546–550. https://doi.org/10.1021/acs.jproteome.2c00594.

(49) Shin, D.; Mukherjee, R.; Grewe, D.; Bojkova, D.; Baek, K.; Bhattacharya, A.; Schulz, L.; Widera, M.; Mehdipour, A. R.; Tascher, G.; Geurink, P. P.; Wilhelm, A.; van der Heden van Noort, G. J.; Ovaa, H.; Müller, S.; Knobeloch, K.-P.; Rajalingam, K.; Schulman, B. A.; Cinatl, J.; Hummer, G.; Ciesek, S.; Dikic, I. Papain-like Protease Regulates SARS-CoV-2 Viral Spread and Innate Immunity. *Nature* **2020**, *587* (7835), 657–662. https://doi.org/10.1038/s41586-020-2601-5.
(50) Jiang, H.; Yang, P.; Zhang, J. Potential Inhibitors Targeting Papain-Like Protease of SARS-CoV-2: Two Birds With One Stone. *Frontiers in Chemistry* **2022**, *10*.
(51) Mellott, D. M.; Tseng, C.-T.; Drelich, A.; Fajtová, P.; Chenna, B. C.; Kostomiris, D. H.; Hsu, J.; Zhu, J.; Taylor, Z. W.; Kocurek, K. I.; Tat, V.; Katzfuss, A.; Li, L.; Giardini, M. A.; Skinner, D.; Hirata, K.; Yoon, M. C.; Beck, S.; Carlin, A. F.; Clark, A. E.; Beretta, L.; Maneval, D.; Hook, V.; Frueh, F.; Hurst, B. L.; Wang, H.; Raushel, F. M.; O'Donoghue, A. J.; de Siqueira-Neto, J. L.; Meek, T. D.; McKerrow, J. H. A Clinical-Stage Cysteine Protease Inhibitor Blocks SARS-CoV-2 Infection of Human and Monkey Cells. *ACS Chem. Biol.* **2021**, *16* (4), 642–650. https://doi.org/10.1021/acschembio.0c00875.
(52) Edwards, A. N.; Blue, A. J.; Conforti, J. M.; Cordes, M. S.; Trakselis, M. A.; Gallagher, E. S. Gas-Phase Stability and Thermodynamics of Ligand-Bound, Binary Complexes of Chloramphenicol Acetyltransferase Reveal Negative Cooperativity. *Anal Bioanal Chem* **2023**, *415* (25), 6201–6212. https://doi.org/10.1007/s00216-023-04891-5.
(53) Kundlacz, T.; Schmidt, C. Deciphering Solution and Gas-Phase Interactions between Peptides and Lipids by Native Mass Spectrometry. *Anal. Chem.* **2023**, *95* (47), 17292–17299. https://doi.org/10.1021/acs.analchem.3c03428.
(54) Nowak, Ł.; Krajewski, W.; Dejnaka, E.; Małkiewicz, B.; Szydełko, T.; Pawlak, A. Ubiquitin-Specific Proteases as Potential Therapeutic Targets in Bladder Cancer—In Vitro Evaluation of Degrasyn and PR-619 Activity Using Human and Canine Models. *Biomedicines* **2023**, *11* (3), 759. https://doi.org/10.3390/biomedicines11030759.
(55) Lin, W.-C.; Chiu, Y.-L.; Kuo, K.-L.; Chow, P.-M.; Hsu, C.-H.; Liao, S.-M.; Dong, J.-R.; Chang, S.-C.; Liu, S.-H.; Liu, T.-J.; Hsu, F.-S.; Wang, K.-C.; Lin, Y.-C.; Chang, C.-C.; Huang, K.-Y. Anti-Tumor Effects of Deubiquitinating Enzyme Inhibitor PR-619 in Human Chondrosarcoma through Reduced Cell Proliferation and Endoplasmic Reticulum Stress-Related Apoptosis. *Am J Cancer Res* **2023**, *13* (7), 3055–3066.
(56) Merkley, E. D.; Rysavy, S.; Kahraman, A.; Hafen, R. P.; Daggett, V.; Adkins, J. N. Distance Restraints from Crosslinking Mass Spectrometry: Mining a Molecular Dynamics Simulation Database to Evaluate Lysine–Lysine Distances. *Protein Science* **2014**, *23* (6), 747–759. https://doi.org/10.1002/pro.2458.
(57) Gong, Z.; Ye, S.-X.; Tang, C. Tightening the Crosslinking Distance Restraints for Better Resolution of Protein Structure and Dynamics. *Structure* **2020**, *28* (10), 1160-1167.e3. https://doi.org/10.1016/j.str.2020.07.010.
(58) Orbán-Németh, Z.; Beveridge, R.; Hollenstein, D. M.; Rampler, E.; Stranzl, T.; Hudecz, O.; Doblmann, J.; Schlögelhofer, P.; Mechtler, K. Structural Prediction of Protein Models Using Distance Restraints Derived from Cross-Linking Mass Spectrometry Data. *Nat Protoc* **2018**, *13* (3), 478–494. https://doi.org/10.1038/nprot.2017.146.
(59) Back, J. W.; de Jong, L.; Muijsers, A. O.; de Koster, C. G. Chemical Cross-Linking and Mass Spectrometry for Protein Structural Modeling. *Journal of Molecular Biology* **2003**, *331* (2), 303–313. https://doi.org/10.1016/S0022-2836(03)00721-6.
(60) Hu, H.; Wang, Q.; Su, H.; Shao, Q.; Zhao, W.; Chen, G.; Li, M.; Xu, Y. Identification of Cysteine 270 as a Novel Site for Allosteric Modulators of SARS-CoV-2 Papain-Like Protease. *Angewandte Chemie* **2022**, *134* (52), e202212378. https://doi.org/10.1002/ange.202212378.

(61) Shao, Q.; Xiong, M.; Li, J.; Hu, H.; Su, H.; Xu, Y. Unraveling the Catalytic Mechanism of SARS-CoV-2 Papain-like Protease with Allosteric Modulation of C270 Mutation Using Multiscale Computational Approaches. *Chemical Science* **2023**, *14* (18), 4681–4696. https://doi.org/10.1039/D3SC00166K.
(62) James, V. K.; Sanders, J. D.; Aizikov, K.; Fort, K. L.; Grinfeld, D.; Makarov, A.; Brodbelt, J. S. Expanding Orbitrap Collision Cross-Section Measurements to Native Protein Applications Through Kinetic Energy and Signal Decay Analysis. *Anal. Chem.* **2023**, *95* (19), 7656–7664. https://doi.org/10.1021/acs.analchem.3c00594.
(63) Wang, L.; Li, M.; Sha, B.; Hu, X.; Sun, Y.; Zhu, M.; Xu, Y.; Li, P.; Wang, Y.; Guo, Y.; Li, J.; Shi, J.; Li, P.; Hu, T.; Chen, P. Inhibition of Deubiquitination by PR-619 Induces Apoptosis and Autophagy via Ubi-Protein Aggregation-Activated ER Stress in Oesophageal Squamous Cell Carcinoma. *Cell Proliferation* **2021**, *54* (1), e12919. https://doi.org/10.1111/cpr.12919.
(64) Seiberlich, V.; Borchert, J.; Zhukareva, V.; Richter-Landsberg, C. Inhibition of Protein Deubiquitination by PR-619 Activates the Autophagic Pathway in OLN-T40 Oligodendroglial Cells. *Cell Biochem Biophys* **2013**, *67* (1), 149–160. https://doi.org/10.1007/s12013-013-9622-8.
(65) Seiberlich, V.; Goldbaum, O.; Zhukareva, V.; Richter-Landsberg, C. The Small Molecule Inhibitor PR-619 of Deubiquitinating Enzymes Affects the Microtubule Network and Causes Protein Aggregate Formation in Neural Cells: Implications for Neurodegenerative Diseases. *Biochimica et Biophysica Acta (BBA) - Molecular Cell Research* **2012**, *1823* (11), 2057–2068. https://doi.org/10.1016/j.bbamcr.2012.04.011.
(66) Soji, K.; Doi, S.; Nakashima, A.; Sasaki, K.; Doi, T.; Masaki, T. Deubiquitinase Inhibitor PR-619 Reduces Smad4 Expression and Suppresses Renal Fibrosis in Mice with Unilateral Ureteral Obstruction. *PLOS ONE* **2018**, *13* (8), e0202409. https://doi.org/10.1371/journal.pone.0202409.
(67) Kuo, K.-L.; Liu, S.-H.; Lin, W.-C.; Chow, P.-M.; Chang, Y.-W.; Yang, S.-P.; Shi, C.-S.; Hsu, C.-H.; Liao, S.-M.; Chang, H.-C.; Huang, K.-H. The Deubiquitinating Enzyme Inhibitor PR-619 Enhances the Cytotoxicity of Cisplatin via the Suppression of Anti-Apoptotic Bcl-2 Protein: In Vitro and In Vivo Study. *Cells* **2019**, *8* (10), 1268. https://doi.org/10.3390/cells8101268.

TOC